

Mechanism of stochastic resonance in viscoelastic channel flow

Yuke Li* and Victor Steinberg†

Department of Physics of Complex Systems, Weizmann Institute of Science, Rehovot 7610001, Israel

(Dated: May 14, 2024)

We have recently discovered stochastic resonance (SR) in chaotic inertia-less viscoelastic channel flow. SR appears just above a pure elastic instability at a critical Weissenberg number, $Wi_c = 150$, of a transition regime. In this lower sub-region up to $Wi \sim 300$, only the streamwise velocity, u , exhibits a chaotic spectrum, E_u , while the spanwise velocity continues to exhibit white noise, verified by its flat spectrum, E_w , accompanied by weak intensity elastic waves. However, SR vanishes at the upper limit at $Wi \sim 300$, when E_w becomes chaotic, indicating Wi as the control parameter. Here we clarify the mechanism of SR emergence by validating the control parameters, namely Wi and the rms velocity fluctuations, u_{rms} , measured at multiple channel locations, which determine the range of SR existence. Our experiments verify three key ingredients of the SR mechanism: chaotic E_u , white noise E_w , and weak elastic waves, which are consistent with three constituents of autonomous dynamical systems exhibiting SR.

In several recent publications we have reported a direct transition from laminar to sustained chaotic flow at $Wi > Wi_c$ and $Re \ll 1$ in inertia-less viscoelastic channel flow. It occurs via a supercritical non-normal mode elastic instability at Wi_c , due to finite-amplitude external white noise perturbations u_{rms} at the inlet $l/h = 0$, despite the proven linear stability of viscoelastic parallel shear flows [1, 2]. Here, the Weissenberg number $Wi = U\lambda/d$ is the main control parameter in inertia-free viscoelastic fluid flow, denoting the ratio of the elastic stress to its relaxation dissipation, where U is the mean flow velocity defined by the fluid discharge rate (see the Supplementary Material [3] and the references [4, 5] therein), $Wi_c = 150 \pm 10$ is the instability onset for the discussed channel, d is the characteristic vessel size, and λ is the longest polymer relaxation time, u_{rms} is a root mean square (rms) of the streamwise velocity fluctuations, l is the location along the channel, and h is the channel height.

The next significant step in uncovering a mechanism to promote chaotic channel flow at $Wi > Wi_c$ in three flow regimes is the proposed and experimentally verified mechanism of vortex amplification by elastic waves [6]. Therefore, the key role of elastic waves in amplifying the wall-normal vortex fluctuations is the resonant pumping of elastic wave energy extracted from the mean shear flow into fluctuating vortices at $Wi > Wi_c$, which requires sufficient elastic wave energy and could be problematic near Wi_c where elastic waves are just initiated. Thus, the goal of our recent study [7] was to uncover the transition to chaotic flow near Wi_c . We increase the resolution near threshold to study flow behaviours near Wi_c . First, this study reveals two sub-regions at $Wi > Wi_c$ in the transition regime: lower at $150 < Wi \leq 300$ and upper at $400 \leq Wi \leq 1000$. In the lower sub-region, the laminar flow becomes chaotic only in the streamwise direction, x , while in the spanwise direction, z , the spanwise velocity, $w(t)$, power spectrum, E_w remains flat indicated white noise fluctuations as at $Wi < Wi_c$ and with low inten-

sity peaks of the elastic waves. In addition, the time series of the streamwise velocity $u(t)$ and pressure $p(t)$ show large and nearly periodic negative spikes. These spikes result in low-frequency, high-energy peaks in the streamwise velocity, E_u , and pressure, E_p , power spectra. As suggested in Ref. [7], the nearly periodic sharp low-frequency and high-energy peaks in E_u and E_p in the lower sub-region resemble stochastic resonance (SR). Moreover, high-energy elastic waves now take over the key role from SR, since they are able to amplify the wall-normal vorticity fluctuations and self-organize the streaks into cycles synchronized at the elastic wave frequency, f_{el} [6]. Thus, SR is the key factor of the stochastic path to the persistent chaotic flow just above Wi_c in the lower sub-region. However, this finding is based only on the study of viscoelastic channel flow at the fixed spatial location $l/h = 380$ [7]. To our knowledge, this marks the first experimental observation of SR in chaotic systems within fluid dynamics.

In the upper sub-region at $400 \leq Wi \leq 1000$, the SR disappears along with the appearance of both E_u and E_w as chaotic power spectra and high intensity elastic waves. Thus, the low-frequency, high-energy SR detected in the lower sub-region ensures the transition from laminar to sustained chaotic flow above Wi_c . This is reminiscent of a scenario that occurs in an autonomous dynamical chaotic system interacting with external white noise in the presence of weak periodic modulation [8, 9]. It differs fundamentally from classical SR, which involves either weak oscillations with external white noise or a bistable system driven by both external noise and a weak periodic signal [10, 11]. In deterministic chaotic systems, quasi-attractors merge into a single chaotic attractor above a critical parameter value in an event known as an attractor crisis [9]. Post-crisis, the merged attractor intermittently switches in a “chaos-chaos” manner, forming a “deterministic stochastic attractor” interacting with external noise. This switching can be synchronized by weak periodic modulation, producing SR at a fixed control param-

eter value [8, 9].

Here we present experimental results obtained in the same inertia-less viscoelastic channel flow and with the same approach as in Ref. [7], where SR is discovered and characterized in the lower sub-region of the transition regime, but at the multiple spatial locations l/h along the channel length, where l/h plays the role of the second controlled parameter besides Wi .

The main goal of the experiment is to verify the mechanism of SR emergence and to validate the control parameter besides Wi , defining the range of SR existence. Moreover, we intend to reveal the relation between elastic wave and SR frequencies, important feature to verify the proposed mechanism of SR appearance.

We performed the experiment in a long channel of dimensions $500 (L, x: \text{streamwise}) \times 0.5 (h, y: \text{wall-normal}) \times 3.5 (W, z: \text{spanwise}) \text{ mm}^3$ in Fig. S1 in [3]. The channel has two sources of finite size perturbations, namely an unsmoothed inlet and two 0.5 mm diameter holes in the top plate near the inlet and outlet used for pressure measurements. A dilute aqueous solution of 64% sucrose concentration and 80 ppm high molecular weight polyacrylamide (PAAm) is the same as that used in Ref. [7]. The longest polymer relaxation time λ is 13 s. The average velocity U , used in both Wi and Re , is obtained via the flow discharge rate, Q , as $U = Q/\rho Wh$. In the Methods in the Supplementary Material [3], we present the details of the experimental setup, the preparation and characterization of the polymer solution, and the Particle Image Velocimetry (PIV) technique to measure the 2D velocity field in the $x - z$ horizontal plane.

In Fig. 1, the left column shows three plots of the temporal evolution of $u_{rms}^p(t)$, the partially averaged over consecutive 1s (100 samples) streamwise velocity fluctuations, at three positions, l/h : (a) 90 at $Wi = 160$; (c) 180 at $Wi = 228$; (e) 960 at $Wi = 172$. The right column shows $u(t)$ power spectra, E_u , in lin-log presentation at the corresponding l/h and various Wi values in the lower sub-region of the transition regime: (b) 90 at $Wi = 160$; (d) 180 at $Wi = 164, 228$; (f) 960 at $Wi = 155, 172, 250$. In Figs. 1(a),(c),(e), the $u_{rms}^p(t)$ time evolution shows almost periodic spikes of the partially smoothed data, whose E_u in Figs. 1(b),(d),(f) show sharp, high energy peaks associated with SR.

In Fig. 2 we show PDFs of $P(u'/u_{rms})$ at $l/h = 150, 720$ and several Wi values in the lower sub-region of the transition regime. As in ref.[7], strong deviations from the Gaussian PDF appear for negative values of u'/u_{rms} for all Wi . It is noteworthy that further down, the deviations of the left tail from the Gaussian PDF become closer to exponential than another shifted Gaussian PDF, as observed at $l/h = 380$ in Fig. 2 in Ref. [7]. The characterization of the PDF shape deviation from Gaussian is quantified by its third and fourth moments, called skewness, S , and flatness (kurtosis), F , respectively, shown in Fig. 4(c) as a function of Wi values

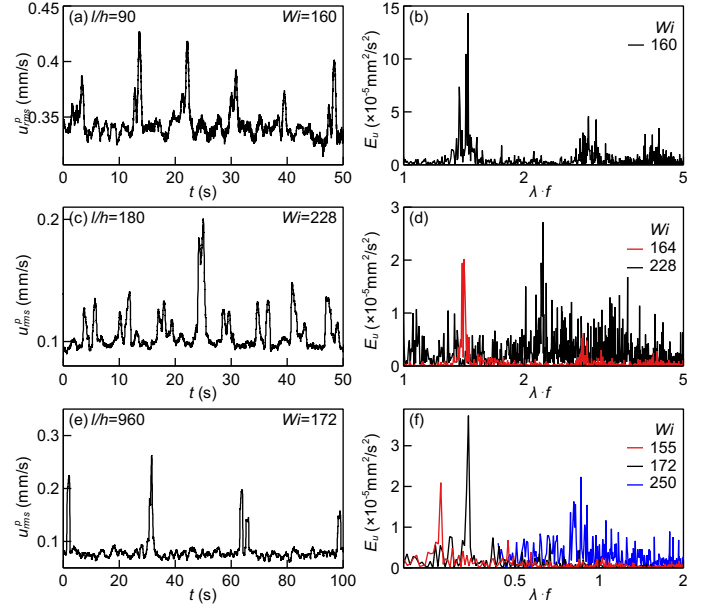


FIG. 1. Partially averaged over each consecutive 1s (100 samples) stream-wise velocity fluctuations, $u_{rms}^p(t)$, and u energy spectra, E_u , at various l/h and Wi values. At $l/h=90$: (a) $u_{rms}^p(t)$ at $Wi=160$ and (b) E_u at $Wi=160$; at $l/h=180$: (c) $u_{rms}^p(t)$ at $Wi=228$ and (d) E_u at $Wi=164$ and 228 ; at $l/h=960$: (e) $u_{rms}^p(t)$ at $Wi=172$ and (f) E_u at $Wi=155, 172$ and 250 .

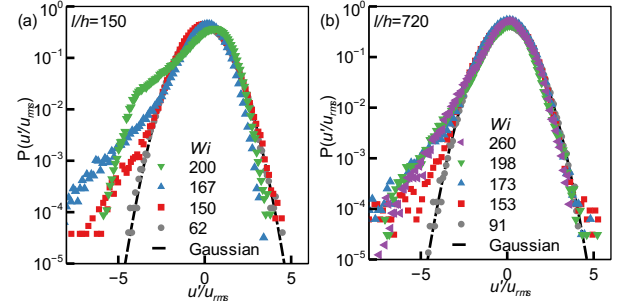


FIG. 2. Probability density functions $P(u'/u_{rms})$, at different l/h and Wi s: (a) at $l/h=150$ and $Wi=62, 150, 167$ and 200 ; and (b) at $l/h=720$ and $Wi=91, 153, 173, 198$ and 260 . The dashed black lines represent the Gaussian PDF.

in the lower sub-region over a wide range of l/h . At $l/h = 380, 720, 960$, sufficiently far from the inlet, both S and F exhibit a non-monotonic dependence on Wi with a smoothed maximum in the middle of the lower sub-region, so that the absolute values of S and F decrease with increasing l/h . Meanwhile, at $l/h = 150$, F grows abruptly above Wi_c and then drops significantly towards $Wi \approx 200$.

As mentioned in the introduction and also in Ref. [7], SR is observed only in the lower sub-region at $l/h = 380$, where the remaining flat spectrum E_w , which denotes white noise versus λf in log-log coordinates, shows a weak growth with Wi . According to the proposed simi-

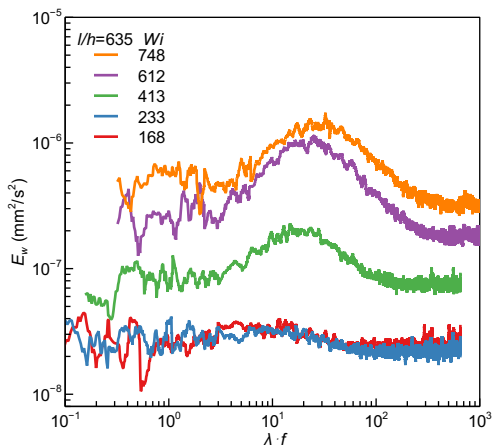


FIG. 3. Spanwise velocity energy spectra in log-log scales measured at the channel center far from the inlet: E_w at $l/h=635$ and $Wi=168, 233, 413, 612$ and 748 .

larity of the SR appearance in the autonomous dynamical chaotic system [8, 9], the interaction of the chaotic attractor with external white noise in the presence of weak oscillations is the necessary condition for the SR appearance. To verify the dependence of E_w on λf at several positions, l/h and various Wi in the lower sub-region of the transition regime are plotted in log-log coordinates for $l/h = 635$ and $Wi = 168, 233, 413, 612, 748$ in Fig. 3 and additionally for $l/h = 22, 62, 90, 180, 840$ and various Wi values in Fig. S3 [3]. The results shown in Fig. 3 and Figs. S3(c),(d),(e) of [3] at l/h from 90 to 840 confirm the observation reported in Ref. [7] that SR is observed only for chaotic E_u interacting with a flat white noise E_w accompanied by weak elastic waves. However, near the inlet at $l/h = 22$, E_w remarkably exhibits chaotic spectra for all Wi values throughout the transition regime in Fig. S3(a) [3]. Similarly, at $l/h = 62$ and 90 E_w remains chaotic except at $Wi = 162$, where E_w is nearly flat. Thus, the SR exists only in the lower sub-region where the flat, white noise E_w is found, as shown by the phase diagram in Wi and l/h coordinates (Fig. S4 [3]). This is the key result first reported at $l/h = 380$ in Ref. [7].

One reason for the dependence of the upper Wi bound of the lower sub-region on l/h , where SR is detected, is the fact that u_{rms}/U and the normalized elastic wave energy, I_{el}/w_{rms}^2 , decrease with l/h at all Wi in the transition regime. It was first observed in a channel with six small holes in a top plate, shown in Fig. 6 of Ref. [12] and Fig. S2 in [3] for the current channel. First, since both u_{rms}/U and I_{el}/w_{rms}^2 persist up to the channel outlet, the non-normal elastic instability due to continuous perturbations at the inlet is absolute (or global), as first pointed out in Ref. [12]. This means that convective (or local) instability is absent, in contrast to Newtonian open flows where an initial convective instability followed by absolute instability is theoretically explained in refs. [13–

15] and experimentally confirmed in refs. [16–20]. As already suggested in Ref. [12], these discrepancies between the properties of Newtonian and viscoelastic open flows are caused by the different nature of the nonlinear terms: Only one advection term in the velocity field in the former versus three nonlinear terms, including one advection term, in the elastic stress field in the latter. Moreover, in contrast to Newtonian open flows, the viscoelastic flow properties depend on l/h above Wi_c in Figs. S2(a), (b) in [3]. Furthermore, the u_{rms}/U dependence on l/h is the same for the lower and upper sub-regions in Fig. S2(a) in [3], while the I_{el}/w_{rms}^2 dependence on l/h is different in both sub-regions in Fig. S2(b) in [3]. Furthermore, both u_{rms}/U and I_{el}/w_{rms}^2 show two distinct regions with similar l/h dependencies: a steep decrease near the inlet and a gentle decrease further away. Near the inlet, the steep decrease of u_{rms}/U due to external perturbations occurs from about 14% down to $\sim 4\%$ at $l/h \approx 90$ and then decreases to $\sim 3\%$ near the outlet. While for I_{el}/w_{rms}^2 the transition locations from steep to gentle slope occur for the lower sub-region at ~ 140 and for the upper sub-region at $l/h \approx 90$, and as a result the steepness for I_{el}/w_{rms}^2 differs for the lower and upper sub-regions far from the inlet in Fig. S2(b) in [3]. To summarize, the observed dependence of the SR existence range and the elastic wave intensity on l/h is due to the dependence of u_{rms}/U on l/h . This means that u_{rms}/U is the second control parameter besides Wi . Thus, one could expect that different values of u_{rms}/U at the inlet would also affect the presence range of SR and flat white noise E_w .

In addition, the SR energy peak, I_p , and the SR normalized frequency, λf_p , observed exclusively in the lower sub-region of the transition regime at various Wi values and ten locations, $l/h = 62, 90, 150, 180, 270, 380, 635, 720, 840, 960$, are shown in Figs. 4(a),(b) and also provided in Table S1 [3]. The SR normalized frequency, λf_p , grows with Wi at all locations, and the fit of all data shows a scaling relationship $\lambda f_p \sim (Wi - Wi_c)^\gamma$ with $\gamma = 0.45 \pm 0.05$, the same as at $l/h = 380$ in Ref. [7]. The I_p shows mostly growth with Wi for all l/h values, and then a slight decrease towards $Wi \approx 300$, the upper limit of the lower sub-region.

In Figs. S5(a), (b) [3] we plot λf_{el} and I_{el} as functions of Wi , at eleven locations $l/h = 22, 62, 90, 150, 180, 270, 380, 635, 720, 840, 960$ in both sub-regions of the transition flow regime. In the lower sub-region, E_w remains flat as discussed above, and I_{el} slowly increases up to the upper limit at $8 \times 10^{-8} (mm^2/s^2)$, marked by the red dotted line for all positions where I_{el} has two orders of magnitude lower energy than I_p (Fig. 4 and Fig. S5(b) [3]). Only for $l/h = 22$ and $l/h = 62$ do the I_{el} values find an order of magnitude larger than the upper limit at $Wi = 162, 235$ and $Wi = 162$, respectively, and remain larger than those at the other locations, although they vary at about the same rate as for the other l/h values. In

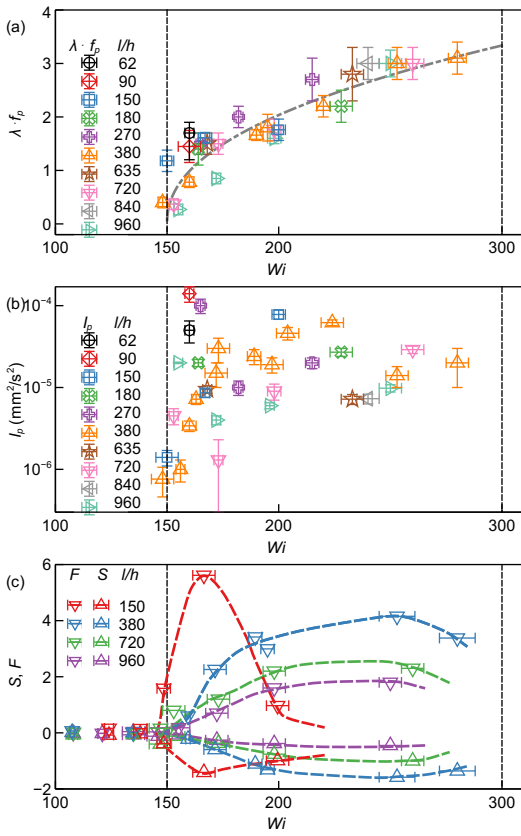


FIG. 4. Properties of spikes near threshold instability in two sub-regions. (a) Normalized SR frequency, $\lambda \cdot f_p$, versus Wi at different l/h . The black dashed line is the power-law fit $\lambda \cdot f_p \sim (Wi - Wi_c)^\gamma$ with $\gamma = 0.45 \pm 0.05$. (b) SR peak energy I_p in E_u versus Wi at the same l/h . (c) Skewness, S , and flatness (kurtosis), F , of $P(u'/u_{rms})$ versus Wi at four l/h values. The colored dashed lines show trends. The vertical black dashed lines in (a-c) mark $Wi_c = 150$ and $Wi=300$, as limits of the lower sub-region.

Fig. S5(a) [3] one finds the growth of λf_{el} with Wi at all positions along the channel, although at $l/h = 22, 62, 90$ λf_{el} remains smaller than the rest in both sub-regions. To compare the scaling of λf_p and λf_{el} versus $Wi - Wi_c$, we plot $\lambda \cdot f_{el} \sim (Wi - 150)^\beta$ with $\beta = 0.4 \pm 0.1$ in the lower sub-region at eleven locations $l/h = 22, 62, 90, 150, 180, 270, 380, 635, 720, 840, 960$ (Fig. S5(a) [3]), which is close to the exponent $\gamma = 0.45 \pm 0.5$ obtained for λf_p in Fig. 4. In the upper sub-region, E_w becomes chaotic with the power-law decay at high frequencies (see Fig. 3 and Figs. S3(a),(b),(c)[3]), and SR disappears. The latter is accompanied by a steep growth of I_{el} , reaching the I_p values observed in the lower sub-region. Moreover, E_w remains flat and grows up to $\sim 10^{-7}(mm^2/s^2)$, close to the resolution limit Table S1 [3].

In summary, we observe a strong dependence of the Wi upper bound of the lower sub-region as a function of l/h near the inlet. At $l/h = 22$ for $Wi = 162$ and 235 , u_{rms}/U is up to 4 times larger, and at $l/h = 62$ and $Wi =$

235 , u_{rms}/U is about twice as large as far downstream. Such large u_{rms}/U values near the inlet lead to chaotic E_w and much larger I_{el} values either at $l/h = 22$ for all $Wi > Wi_c$ or at $l/h = 62$ and 90 in the upper limit at $Wi = 162$, close to Wi_c . This means that the range of existence of SR and flat white noise E_w depends on the value of u_{rms}/U . To verify the relation between SR and elastic waves, we show that the exponents β and γ in the scaling relations of f_{el} and f_p on $Wi - Wi_c$ have close values of 0.45 ± 0.5 and 0.4 ± 0.1 within the error bar, proving their direct relation. However, the range of λf_p is significantly shifted down four to five times compared to the range of f_{el} (Fig. 4(a) versus (Fig. S5(a) [3]), which is in contrast to the dynamical chaotic model with f_p shifted up relative to f_{el} , and its value is determined by the noise strength [8, 9].

In conclusion, SR appears exclusively in the lower sub-region of the transition flow regime just above Wi_c . There are three key factors that define the range of SR existence: (i) the presence of flat white noise E_w , (ii) low-intensity elastic waves, and (iii) the presence of u_{rms}/U , the second control parameter besides Wi . When E_w becomes chaotic, SR ceases to exist because the mechanism of SR generation is no longer effective. The next crucial observation is the same scaling dependence of both frequencies, f_p and f_{el} , on $Wi - Wi_c$, indicating the direct relationship between SR and elastic waves, although f_p is shifted down 4-5 times relative to f_{el} . Thus, these two basic observations are the critical ingredients that allow the use of the autonomous dynamical model, where the chaotic attractor interacts with external noise in the presence of limit cycles (oscillations) leading to SR, with the experimental findings in the much more involved viscoelastic channel flow. We have to note that our experimental observations are obtained in a flow with infinite degrees of freedom, in contrast to the autonomous dynamical chaotic model [8, 9].

In the lower sub-region above Wi_c , SR takes the role of elastic waves whose energy peak I_{el} is more than two orders lower than I_p . As a result, SR initiates the appearance of random streaks and wall-normal vortex fluctuations by transferring energy from the main flow to the vortex fluctuations. When E_w becomes chaotic at higher Wi , I_{el} also increases significantly to take over the role of a driving factor to promote self-organization of streak cycles synchronized by the elastic wave frequency, f_{el} , and to amplify wall-normal vortex fluctuations via the mechanism previously described and verified by us [6].

We thank Guy Han and Rostyslav Baron for their help with the experimental setup. This work was partially supported by the Israel Science Foundation (ISF, grant #784/19).

* yuke.li@weizmann.ac.il

† victor.steinberg@weizmann.ac.il

- [1] V. A. Gorodtsov and A. I. Leonov, On a linear instability of a plane parallel couette flow of viscoelastic fluid, *J. Appl. Math. Mech.* **31**, 289 (1967).
- [2] M. Renardy and Y. Renardy, Linear stability of plane couette flow of an upper convected maxwell fluid, *J. Non-Newton. Fluid Mech.* **22**, 23 (1986).
- [3] See Supplemental Material [url] for Methods details and supplementary figures and table, which includes Refs. [7,8].
- [4] Y. Liu, Y. Jun, and V. Steinberg, Concentration dependence of the longest relaxation times of dilute and semi-dilute polymer solutions, *J. Rheol.* **53**, 1069 (2009).
- [5] A. Liberzon, T. Käufer, A. Bauer, P. Vennemann, and E. Zimmer, Openpiv/openpiv-python: Openpiv-python v0.23.3., 10.5281/zenodo.4320056 (2020).
- [6] Y. Li and V. Steinberg, Mechanism of vorticity amplification by elastic waves in a viscoelastic channel flow, *Proc. Nat. Acad. Sci. U. S. A.* **120**, e2305595120 (2023).
- [7] Y. Li and V. Steinberg, From laminar to chaotic flow via stochastic resonance in viscoelastic channel flow, e-print arXiv:2404.09508 (2024).
- [8] V. S. Anishchenko, A. B. Neiman, and M. A. Safanova, Stochastic resonance in chaotic systems, *J. Stat. Phys.* **70**, 183 (1993).
- [9] V. S. Anishchenko, A. B. Neiman, F. Moss, and L. Shimansky-Geier, Stochastic resonance: noise-enhanced order, *Physics-Uspokhi* **42**, 7 (1999).
- [10] R. Benzi, A. Sutera, and A. Vulpiani, The mechanism of stochastic resonance, *J. Phys.* **14A**, L451 (1981).
- [11] L. Gammaitoni, P. Hänggi, P. Jung, and F. Marchesoni, Stochastic resonance, *Rev. Mod. Phys.* **70**, 223 (1998).
- [12] Y. Li and V. Steinberg, Universal properties of non-hermitian viscoelastic channel flows, *Sci. Rep.* **13**, 1064 (2023).
- [13] D. Barkley, Theoretical perspective on the route to turbulence in a pipe, *J. Fluid Mech.* **803**, P1 (2016).
- [14] P. Huerre and P. A. Monkevitz, Local and global instabilities in spatially developing flows, *Annu. Rev. Fluid Mech.* **22**, 473 (1990).
- [15] J.-M. Chomaz, Instabilities in spatially developing flows: Non-normality and nonlinearity, *Annu. Rev. Fluid Mech.* **37**, 357 (2005).
- [16] A. Tsameret and V. Steinberg, Convective vs. absolute instability in couettetaylor flow with an axial flow, *Euro. Phys. Lett.* **14**, 331 (1991).
- [17] A. Tsameret and V. Steinberg, Noise-modulated propagating pattern in a convectively unstable system, *Phys. Rev. Lett.* **67**, 3392 (1991).
- [18] K. Babcock, G. Ahlers, and D. Cannell, Noise-sustained structure in taylor-couette flow with through flow, *Phys. Rev. Lett.* **67**, 3388 (1991).
- [19] K. Babcock, D. Cannell, and G. Ahlers, Stability and noise in taylor-couette flow with through-flow, *Physica D* **61**, 40 (1992).
- [20] A. Tsameret and V. Steinberg, Absolute and convective instabilities and noise sustained structures in couette-taylor system with an axial flow, *Phys. Rev. E* **49**, 1291 (1994).

Supplementary Materials

for the article “ Mechanism of stochastic resonance in viscoelastic channel flow”

Yuke Li, Victor Steinberg*

Department of Physics of Complex Systems, Weizmann Institute of Science, Rehovot
7610001, Israel

victor.steinberg@weizmann.ac.il *

Experimental setup and Methods

The experiments are carried out in a straight channel with a rectangular cross-section, made of acrylic and screwed to a metal frame. The dimensions of the channel are 500 mm in the streamwise direction (L, x), 3.5 mm in the spanwise direction (W, z) and 0.5 mm in the vertical (wall-normal) direction (h, y), giving a total volume of $500 \times 3.5 \times 0.5 \text{ mm}^3$, as shown in Fig. S1. The polymer solution for the experiment is stored in a large stainless steel container and is driven by compressed nitrogen gas, controlled by pressure regulators. As the fluid exits the container, it first passes through two right-angled bends before flowing into the channel and is then collected in a glass container mounted on a balance (BPS-1000-C2-V2, MRC) at the outlet. The flow discharge is measured instantaneously as a function of time, $m(t)$, using the PC-interfaced balance. The time-averaged fluid discharge rate is calculated as $Q = \langle \Delta m / \Delta t \rangle$, which is used to obtain the mean velocity $U = Q / \rho Wh$, used in both $Wi = \lambda U / h$ and $Re = \rho U h / \eta$.

Two-dimensional Particle image velocimetry (PIV) is used in $x - z$ plane to measure the velocity profile and fluctuations. The fluid is seeded with $3.2 \mu\text{m}$ particles of $\sim 1\%$ w/w concentration (Thermo Scientific) and illuminated by a laser sheet of approximately $50 \mu\text{m}$ thickness. Images are taken with a high speed, high spatial resolution camera (Mini WX100 FASTCAM, Photron) through a 4X objective. For velocity fluctuation measurements we take a small window of $256 \times 96 \text{ px}^2$ as a single point at the channel center, while for velocity profile measurements we enlarge the window up to $1280 \times 1280 \text{ px}^2$. The window size for PIV is $32 \times 32 \text{ px}^2$ with 50% overlap with 200% search window size. The OpenPIV software [1] is used to analyze $u(x, z, t)$ and $w(x, z, t)$ in the $x-z$ plane to record data for $\sim \mathcal{O}(15)$ minutes, or $\sim \mathcal{O}(50\lambda)$, for each Wi to obtain sufficient statistics.

The working fluid is a dilute solution of the high molecular weight polyacrylamide (PAAm) with $M_w = 18 \text{ MDa}$. The Newtonian solvent consists of 64% sucrose and 1% NaCl dissolved in water. By adding a PAAm concentration of $c = 80 \text{ ppm}$ ($c/c^* \approx 0.4$ with the overlap PAAm concentration $c^* \approx 200 \text{ ppm}$ [2]) to the solvent, we obtain viscoelastic working fluid. The properties of the solution include a density of $\rho = 1320 \text{ kg/m}^3$, and solvent and solution viscosities of $\eta_s = 0.13 \text{ Pa}\cdot\text{s}$ and $\eta = \eta_s + \eta_p = 0.17 \text{ Pa}\cdot\text{s}$, respectively, $\eta_s / (\eta_s + \eta_p) = 0.765$, where η_p is the polymer contribution to the solution viscosity, and the longest polymer relaxation time of $\lambda = 13 \text{ s}$, obtained by the stress relaxation method [2].

Supplementary figures

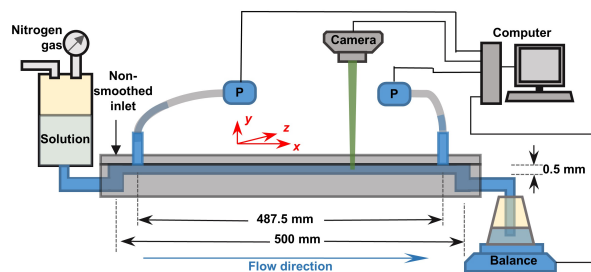


Fig. S 1: Schematic of the experimental set-up. The polymer solution is stored in a large stainless steel vessel and is driven by compressed nitrogen gas controlled by pressure regulators. The solution flows through a straight channel with a unsmoothed inlet and two small holes in the top wall. The solution exiting the outlet is collected in a beaker on the balance. The two holes provide the pressure measurement, and the balance measures the flow discharge rate. Seeded tracers are illuminated by a thin laser sheet along $x - z$ plane at the center of the channel and a high speed camera is used for image acquisition.

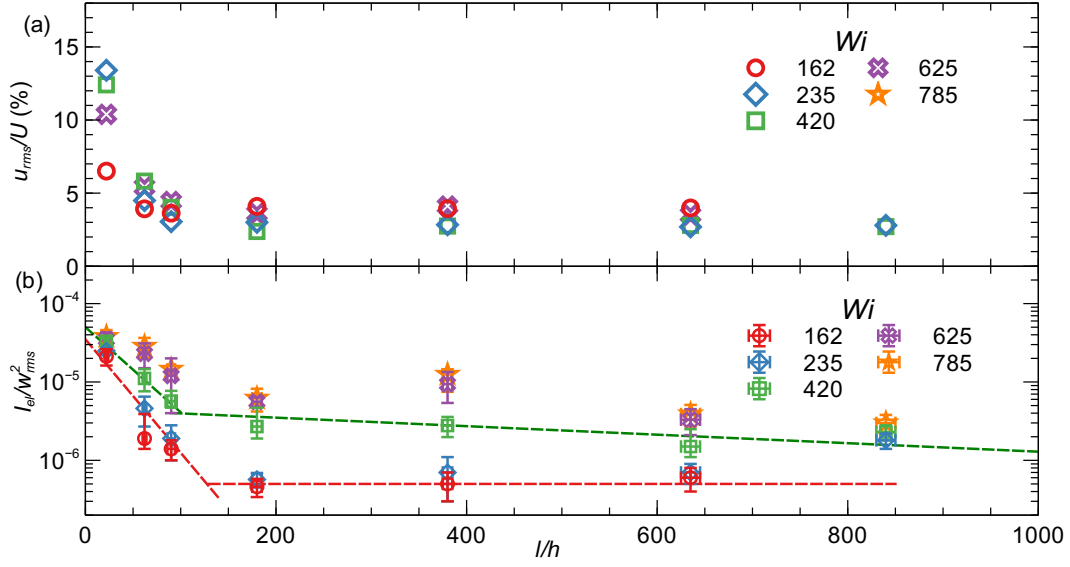


Fig. S 2: (a) Normalized streamwise velocity fluctuations, u_{rms}/U , and (b) elastic wave energy, I_{el} normalized by the square of the spanwise velocity fluctuations, I_{el}/w_{rms}^2 , versus different downstream locations from the inlet, l/h , at five different Wi in the transition flow regime. The red dashed lines in (b) show the decay for the lower sub-range, while the green lines show the decay for the upper sub-range.

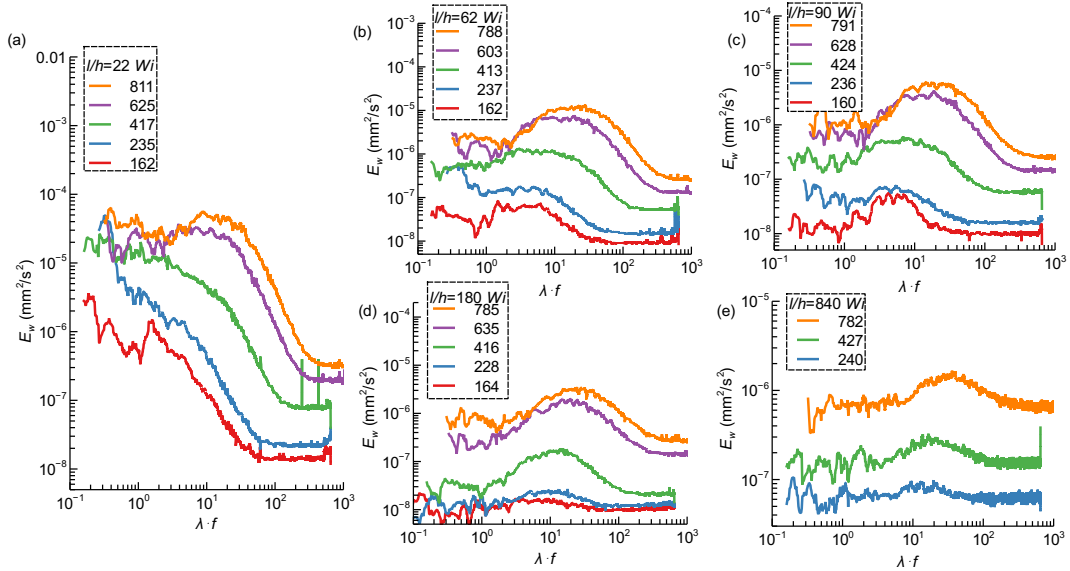


Fig. S 3: Spanwise velocity spectrum, E_w , versus normalized frequency, $\lambda \cdot f$, at five downstream locations, $l/h=22, 62, 90, 180$ and 840 , and several Wi values in the transition flow regime.

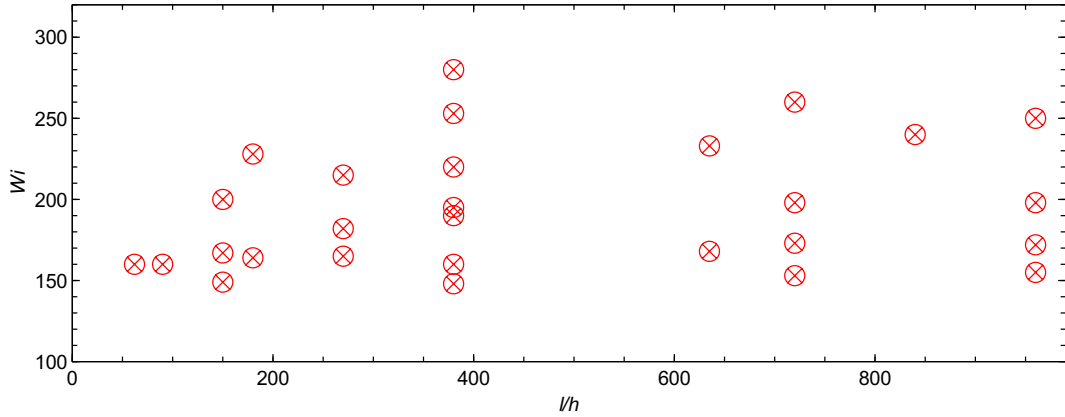


Fig. S 4: Stochastic resonance peaks found in the lower sub-range are shown in l/h and Wi coordinates.

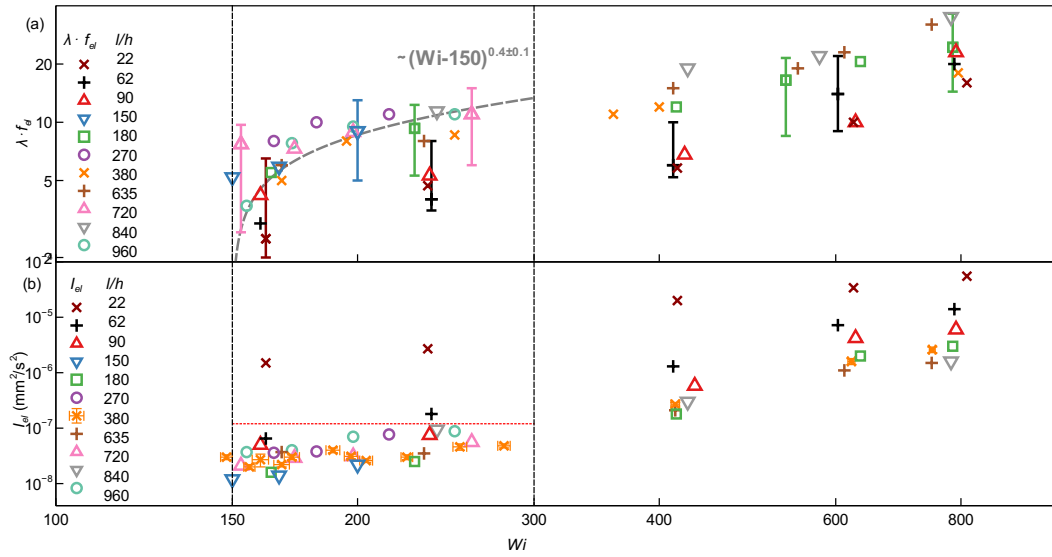


Fig. S 5: (a) Normalized elastic wave frequency, $\lambda \cdot f_{el}$, and (b) elastic wave energy, I_{el} , versus Wi at several downstream locations, $l/h = 22, 62, 90, 180, 270, 380, 635, 720, 840,$ and 960 . $\lambda \cdot f_{el}$ is plotted with selected error bars. The dashed line is the power-law fit $\lambda \cdot f_{el} \sim (Wi - 150)^\beta$ with $\beta = 0.4 \pm 0.1$. The vertical black dashed lines indicate $Wi_c = 150$, and $Wi = 300$, the approximate upper limit of the lower sub-range of the transition flow regime, where the SR energy, I_p , exceeds the elastic wave energy, I_{el} , by up to two orders of magnitude and drives chaotic flow. The horizontal red dotted line in (b) indicates the limit above which the elastic wave energy is sufficient to take over.

Supplementary table

Table S1: Table comparing the streamwise spike intensity, I_p , and the spanwise elastic wave intensity, I_{el} . The rows in light green are for the lower sub-range, while the rows in light yellow are for the upper sub-range in the transition regime. I_{el} is also calculated on the smoothed spanwise spectrum because the elastic wave peaks are broad and noisy. Plots of these data are also shown in Fig. 4(b), Fig. S2(b) and Fig. S5(b).

l/h	Wi	I_p (mm^2/s^2)		I_{el} (mm^2/s^2)	
		raw		raw	averaged
22	162			5.6e-6	1.5e-6
22	235			5.7e-6	2.7e-6
22	417			3.7e-5	2e-5
22	625			1.8e-4	3.4e-5
22	811			4e-4	5.5e-5
62	162	5e-5		3.3e-7	6.5e-8
62	237			8.6e-7	1.8e-7
62	413			6.1e-6	1.3e-6
62	603			3.5e-5	7.2e-6
62	788			8e-5	1.4e-5
90	160	1.4e-4		3.6e-7	5e-8
90	236			4.2e-7	7.5e-8
90	434			3.3e-6	5.8e-7
90	628			2.1e-5	4.2e-6
90	791			3.5e-5	6e-6
150	150	1.4e-6		5.6e-8	1.2e-8
150	167	8.6e-6		9e-8	1.4e-8
150	200	7.8e-5		1.5e-7	2.2e-8
180	164	2e-5		1e-7	1.6e-8
180	228	2.7e-5		1.5e-7	2.5e-8
180	416			1.1e-6	1.8e-7
180	635			1.1e-5	2e-6
180	785			2.1e-5	3e-6
270	165	1e-4		2.3e-7	3.6e-8
270	182	1e-5		2.8e-7	3.8e-8
270	215	2e-5		5e-7	7.7e-8
380	148	7.6e-7		1.6e-7	3e-8
380	156	1e-6		1.1e-7	2e-8
380	160	3.4e-6		1.2e-7	2.7e-8
380	168	7.2e-6		8.8e-8	2.2e-8
380	172	1.5e-5		1.6e-7	3e-8
380	189	2.4e-5		2.5e-7	4e-8
380	197	1.9e-5		1.8e-7	3.1e-8
380	204	4.6e-5		1.4e-7	2.6e-8
380	224	6.2e-5		1.6e-7	3e-8
380	253	1.4e-5		2.7e-7	4.6e-8
380	280	2e-5		3e-7	4.8e-8
380	415			1.6e-6	2.7e-7
380	622			8.8e-6	1.6e-6

380	749		1.5e-5	2.6e-6
635	168	9.5e-6	2.9e-7	3.7e-8
635	233	7.2e-6	2.7e-7	3.5e-8
635	415		1.2e-6	2.1e-7
635	612		9e-6	1.1e-6
635	748		1.2e-5	1.5e-6
720	153	4.5e-6	1.2e-7	2.1e-8
720	173	1.2e-6	1.6e-7	2.9e-8
720	198	7e-6	1.8e-7	3.1e-8
720	260	3e-5	3.5e-7	5.6e-8
840	240	7.3e-6	9.6e-8	9.4e-8
840	427		1.9e-6	3e-7
840	782		1e-5	1.6e-6
960	155	2e-5	2e-7	3.7e-8
960	172	3.7e-5	2.7e-7	4e-8
960	198	4e-6	3.5e-7	7e-8
960	250	2e-5	4.5e-7	8.8e-8

References

- [1] A. Liberzon, T. Käufer, A. Bauer, P. Vennemann and E. Zimmer. OpenPIV/openpiv-python: OpenPIV-Python v0.23.3. 10.5281/zenodo.4320056 (Zenodo, 2020)
- [2] Y. Liu, Y. Jun and V. Steinberg. Concentration dependence of the longest relaxation times of dilute and semi-dilute polymer solutions. *J. Rheol.* **53** 1069 (2009)